Published in final edited form as:
Nat Phys. 2019 January ; 15(1): 17–21. doi:10.1038/s41567-018-0301-y.

Wavelength-scale errors in optical localization due to spin-orbit coupling of light

G. Araneda[#1,†], **S. Walser**[#2], **Y. Colombe**[1], **D. B. Higginbottom**[1,3], **J. Volz**[2,‡], **R. Blatt**[1,4], and **A. Rauschenbeutel**[2,5,§]

[1]Institut für Experimentalphysik, Universität Innsbruck, Technikerstraße 25, 6020 Innsbruck, Austria

[2]Vienna Center for Quantum Science and Technology, TU Wien-Atominstitut, Stadionallee 2, 1020 Vienna, Austria

[3]Centre for Quantum Computation and Communication Technology, Research School of Physics and Engineering, The Australian National University, Canberra ACT 2601, Australia

[4]Institut für Quantenoptik und Quanteninformation, Österreichische Akademie der Wissenschaften, Technikerstraße 21a, 6020 Innsbruck, Austria

[5]Department of Physics, Humboldt-Universität zu Berlin, 10099 Berlin, Germany

[#] These authors contributed equally to this work.

Abstract

Far-field optical imaging techniques allow the determination of the position of point-like emitters and scatterers [1–3]. Although the optical wavelength sets a fundamental limit to the image resolution of unknown objects, the position of an individual emitter can in principle be estimated from the image with arbitrary precision. This is used for example in the determination of stars position [4] or in optical super-resolution microscopy [5]. Furthermore, precise position determination is an experimental prerequisite for the manipulation and measurement of individual quantum systems, such as atoms, ions, and solid-state-based quantum emitters [6–8]. Here we demonstrate that spin-orbit coupling of light in the emission of elliptically polarized emitters can lead to systematic, wavelength-scale errors in the estimation of the emitters position. Imaging a single trapped atom as well as a single sub-wavelength-diameter gold nanoparticle, we

[†]Electronic address: gabriel.araneda-machuca@uibk.ac.at. [‡]Electronic address: juergen.volz@tuwien.ac.at. [§]Electronic address: arno.rauschenbeutel@hu-berlin.de.

Author contributions

J.V. and A.R. proposed the concept. All authors contributed to the design and the setting-up of the experiments (atom experiment: G.A., Y.C., D.B.H., and R.B.; nanoparticle experiment: S.W., J.V., and A.R.). G.A. and D.B.H. performed the atom experiment and analysed the data. S.W. performed the nanoparticle experiment and analysed the data. All authors contributed to the writing of the manuscript.

Data availability

The data that support the findings of this study are available from the authors upon reasonable request. Contact persons are G.A. for the ion experiment, J.V. or A.R. for the nanoparticle experiment.

Competing financial interests

The authors declare no competing financial interests.

Europe PMC Funders Author Manuscripts

demonstrate a shift between the emitters measured and actual positions which is comparable to the optical wavelength. For certain settings, the expected shift can become arbitrarily large. Beyond optical imaging techniques, our findings could be relevant for the localization of objects using any type of wave that carries orbital angular momentum relative to the emitters position with a component orthogonal to the direction of observation.

A diffraction-limited imaging system with aperture diameter D has an angular resolution λ/D where λ is the wavelength of the imaging light. Objects with smaller angular diameter cannot be resolved and produce an image given by the point-spread function (PSF) of the optical system. In spite of this limit, fitting the PSF to the image allows one to estimate its position with a precision limited only by the image's signal to noise ratio [9]. The central assumption of this method is that the emitters' positions in the object plane correspond to the centroid of the PSF measured in the image plane, provided that the optical system is focussed.

It is known that the centroid of the image can be affected by imperfect focussing when the emission pattern of the object is anisotropic, as for a linear dipole. Depending on the orientation of the latter, this may lead to lateral shifts of a few tens of nanometres, *i.e.*, much smaller than the diffraction limit [10, 11]. The resulting localization error can be reduced using polarization analysis [12–14] or dedicated PSF fitting [10, 15–17], and vanishes for a focused image. Localization errors of comparable magnitude can occur when the emission pattern is distorted by near-field coupling to a nanoantenna [18, 19].

Here we show that methods for position estimation of emitters can be subject to large fundamental systematic errors when imaging elliptically polarized emitters as a consequence of spin-orbit coupling in the emitted light field. These errors are present even for ideal, *i.e.*, diffraction-limited aberration-free far-field imaging systems. Imaging a single trapped atomic ion as well as a single gold nanoparticle that emits light with different elliptical polarizations, we demonstrate a wavelength-scale shift between the measured and actual positions of the emitter. For a wide range of polarizations, this shift is nearly independent of the numerical aperture. However, it can become arbitrarily large for certain polarizations and vanishing numerical aperture. These findings reveal that, even for small numerical apertures, the paraxial approximation is fundamentally inadequate in the context of the centroid estimation method.

In order to understand the physical origin of the image shift, let us consider a circularly polarized dipole emitter rotating in the x–y plane, at the centre $\mathcal{O}$ of the coordinate system. In this case, the total angular momentum carried by an emitted photon with respect to $\mathcal{O}$ is $\pm\hbar e_z$, where ± corresponds to right-handed (σ^+-) or left-handed (σ^--) polarization of the dipole relative to the z axis, respectively. This total angular momentum can be decomposed into spin and orbital angular momentum, represented by the operators $\hat{S}_z$ and $\hat{L}_z$, respectively. The spin and angular momentum components of the dipole field are coupled and their expectation values for a $\sigma^{\pm}$-polarized dipole are

$$\langle \hat{S}_z \rangle = \pm\hbar \frac{2\cos^2\theta}{1+\cos^2\theta}, \quad \langle \hat{L}_z \rangle = \pm\hbar \frac{\sin^2\theta}{1+\cos^2\theta}, \quad (1)$$

where θ is the angle between the z axis and the direction of observation [20, 21]. In the x–y plane ($\theta = 90°$), the photons carry exclusively orbital angular momentum with expectation value $\pm\hbar$ while the spin angular momentum vanishes, corresponding to linear polarization. This is an example of spin-orbit coupling of light [22] which gives rise to intriguing phenomena such as spin-Hall effect of light [23, 24] and chiral interactions between light and matter [25]. For the circularly polarized dipole field, orbital angular momentum manifests as spiral wavefronts in the x–y plane, see Methods. Hence, the local wavevectors are tilted with respect to the radial direction (see Fig. 1) and the linear momentum per photon has an azimuthal component with expectation value $\langle \hat{p}_\phi(r) \rangle = \langle \hat{L}_z \rangle / r = \pm\hbar/r$. Due to this tilt, the photons seem to originate from a position that is offset from the emitter [21, 26], a fact already predicted by Charles G. Darwin more than 80 years ago [27].

To quantify this shift for a typical far-field imaging system, we consider a circularly polarized dipole emitter located at the front focal point of a lens with focal length f, centred on the x axis. The lens collimates the light and changes its wavevector distribution. However, the mean wavevector $\langle \boldsymbol{k} \rangle$ averaged over the aperture is conserved and the collimated light propagates at an angle

$$\alpha_{\text{tilt}} = \frac{\langle \hat{p}_\phi \rangle_A}{\hbar k} \simeq \pm\frac{\lambda}{2\pi f} \quad (2)$$

with respect to the optical axis. Here, $\langle \cdot \rangle_A$ denotes the expectation value per photon within the aperture A of the lens. The centroid of the intensity distribution at a screen placed at a distance d behind the lens is shifted in the y direction by $\langle y \rangle = \alpha_{\text{tilt}} d$ (Fig. 1) and the apparent y position of the dipole in the object plane is shifted by

$$\Delta y = -\frac{f}{d}\langle y \rangle = \mp\frac{\lambda}{2\pi}. \quad (3)$$

This expression holds for any imaging system, replacing f/d by the magnification factor of the system. To summarize, the light emitted by a circularly polarized $\sigma^\pm$ dipole carries orbital angular momentum due to the optical spin-orbit interaction. When imaging in the plane of polarization of the dipole, this gives rise to a $\mp\lambda/(2\pi)$ shift of the apparent position of the emitter.

We now generalize the above for an elliptically polarized emitter oscillating in the x–y plane. Its polarization state can be written as a superposition of σ^+- and σ^-- polarizations $|\psi\rangle = \alpha|\sigma^+\rangle + \beta|\sigma^-\rangle$, with $|\alpha|^2 + |\beta|^2 = 1$. For a small numerical aperture NA = $D/(2f) \ll 1$, the shift of the apparent position of the emitter is (see Methods)

$$\Delta y = -\frac{\lambda}{2\pi}\cdot\frac{\Re(\epsilon)}{1+\mathrm{NA}^2|\epsilon|^2/2} \quad (4)$$

where the *dipole polarization ratio*, $\epsilon = (\alpha+\beta)/(\alpha-\beta)$, is in general complex and $\Re(\cdot)$ denotes the real value. For σ^+-polarization (σ^--polarization) $\epsilon = +1$ ($\epsilon = -1$) and for linear polarization along the y axis (x axis) $\epsilon = 0$ ($\epsilon = \infty$). For circular polarization and NA $\ll 1$ we recover the $\mp\lambda/(2\pi)$ shift derived above. When the axes of the polarization ellipse coincide with the x and y axes, ϵ is real and the shift is given by

$$\Delta y \simeq -\epsilon\frac{\lambda}{2\pi}, \quad (5)$$

as long as $|\epsilon| \ll 1/\mathrm{NA}$. Outside of this linear regime, the shift reaches a maximum $\Delta y_{\max} = \mp\lambda/(\sqrt{8}\pi\mathrm{NA})$ for $\epsilon = \pm\sqrt{2}/\mathrm{NA}$. Remarkably, this implies that the shift of the apparent position of the emitter can take arbitrarily large positive and negative values for small numerical apertures. For example, with NA = 0.23, the distance between the two extremal shifts is as large as the optical wavelength λ. These large shifts are reached for $\epsilon = \pm 6.3$, *i.e.*, when the polarization of the dipole is almost linear along the optical axis of the imaging system. In this case, the corresponding expectation values of the local orbital angular momentum per photon at the aperture significantly exceed $\hbar$, the total angular momentum per emitted photon. Such 'supermomentum' [28] is an example of weak value amplification common to structured optical fields, in which the local expectation value of an operator can take values outside its eigenspectrum where the field is weak [29, 30]. We note that there is a close connection between the observed weak value amplification and the appearance of momentum vortices in the emitted light field. This connection is shown in Supplementary Fig. 3 which plots the field distribution of the emitted light for different polarization states of the emitter. The plots also provide a graphical illustration for the polarization ratio ϵ which yields the maximum shift of the apparent position: This maximum shift is reached once the momentum vortices enter the field collected by the imaging lens. The centroid determination can be interpreted as a measurement of the weak value of the photons' orbital angular momentum (see Methods). Finally, we note that the predicted shifts also occur for large numerical apertures and that Eq. (5) remains approximately valid provided that $|\epsilon| \lesssim 1$ (see Methods).

We study the predicted shifts by imaging a single atom —a fundamental quantum emitter— and a single sub-wavelength scale nanoparticle. In the first experiment, we confine a $^{138}Ba^+$ atomic ion in a Paul trap and image fluorescence from the dipole transition at $\lambda_1 = 493.41$ nm (Fig. 2a) using an imaging system with magnification $M_a = 5.40(7)$ and NA = 0.40 (see Methods). A bandpass filter and a polarizer are used to collect light selectively from one of the spontaneous decay channels of the excited state, corresponding to the emission from either a σ^+ or a σ^- dipole (see Methods).

Europe PMC Funders Author Manuscripts

We estimate the emitter's position from each image by fitting a 2D Gaussian function, which is a suitable approximation to the PSF in the measured regime [31] (see Methods). Fig. 3a-c show the results for a total measurement time of 3 hours. We observe a displacement between the σ^+ and σ^- emissions of 158(4) nm in the object plane, in agreement with the expected value $\lambda_1/\pi = 157.1$ nm.

As it is demanding to generate an arbitrarily polarized emission from a single atom, we extend the study to the case of a general elliptical polarization in a separate experiment where we image the light scattered by a single sub-wavelength-sized spherical gold nanoparticle. Such particles are used as labelling agents for super-resolution microscopy in biological research [32, 33]. Being a spherically symmetric emitter, the polarization of a nanoparticle's dipole always coincides with the polarization of the illuminating field, which can be controlled precisely. We place a 100 nm-diameter gold nanoparticle in the centre of a glass sphere with refractive index $n = 1.46$ by depositing it on an optical nanofibre [34] and surrounding it by two fused silica 2.5 mm-radius hemispherical solid immersion lenses. The ~ 200 μm gap between the lenses is filled with index matching oil to prevent any reflection near the particle from either the nanofibre or the lenses. The nanoparticle is illuminated by a laser beam (vacuum wavelength $\lambda_2 = 685$ nm) with adjustable polarization and the scattered light is imaged onto a CCD camera through the sphere and a microscope (Fig. 2b). To test the dependence of the position shift on the NA, two different microscope objectives are used with the same nominal magnification but different numerical apertures, resulting in NA = 0.41 and NA = 0.61 when including the silica sphere, and magnifications 21.9(2) and 20.1(1), respectively. The apparent displacement of the nanoparticle is measured by fitting a 2D Gaussian function to its image (see Methods), using alternatively the beam with adjustable polarization and a linearly polarized reference beam. The measurements, averaged over 125 individual realisations for each polarization setting, are shown in Fig. 3. For $|\epsilon| < 2$, within our experimental errors, we observe a very good agreement of our measurements with the expected linear increase of the displacement with ϵ, independent of the numerical aperture. For larger $|\epsilon|$, the linear approximation is not valid and the experimental data follow approximately the theoretical prediction from Eq. (4) (dashed lines). The apparent positions of the nanoparticle imaged with right and left circular polarizations ($\epsilon = \pm 1$) are displaced relative to each other by 145(6) nm for NA = 0.41 and 146(4) nm for NA = 0.61, in agreement with the expected value $2\,\Delta y = \tilde{\lambda}_2/\pi \approx 150\,\text{nm}$, where $\tilde{\lambda}_2 = \lambda_2/n$ is the laser wavelength in the index matching oil. The displacement increases for larger values of $|\epsilon|$, and the total displacement between counter-rotating elliptical polarizations reaches 430(7) nm $\left(\simeq \tilde{\lambda}_2\right)$ for $\epsilon = \pm 5.67$, a shift four times larger than the diameter of the gold nanoparticle. In order to verify that focusing errors are not at the origin of the effect, we slightly defocus our imaging optics and observe that, in the measured range, the shifts do not depend on the distance of the particle to the focal plane (see Methods).

Our findings may affect super-resolution microscopy techniques. The maximum systematic shift due to dipole ellipticity is proportional to the PSF size, which is up to two orders of magnitude larger than the resolution achieved by super-resolution microscopy [35, 36]. For instance, the determination of the position of an emitter with NA = 1, at a wavelength of $\lambda \approx$

628 nm with an accuracy of 1 nm, requires the scattered light to be more than 99.99 % linearly polarized ($|\mathcal{R}(\epsilon)| < 0.01$, see supplementary information). For larger ϵ, an accuracy of, *e.g.*, 1 nm could still be reached by employing an algorithm that not only uses position but also polarization of the dipole as fit parameters for the recorded point-spread function. However, in order to reach the necessary signal-to-noise ratio, this higher dimensional fit requires one to increase the light-collection time by more than 4 orders of magnitude compared to the case of an optimally coupled linear dipole (see supplementary Fig. 4d).

On the positive side, the polarization-dependent shift could be used, *e.g.*, in arrays of optically trapped particles [37], where the apparent location of each particle would give access to the local polarization of an inhomogeneous exciting field; conversely, in the case of an homogeneous exciting field, the shift would allow to sense local physical parameters affecting the polarizability of the particles, such as the direction of the magnetic field. The demonstrated effect is relevant beyond optical imaging, as it will occur for any kind of wave carrying transverse orbital angular momentum. Thus, it may affect the localization of remote objects imaged with radar or sonar techniques [38, 39], or even alter the apparent position of astronomical objects detected through their emission of gravitational waves [40, 41].

Methods

Momentum and wavefronts of the radiated field

The electric field emitted by an optical dipole located at the origin ($r = 0$) that oscillates with angular frequency ω is given by

$$\boldsymbol{E}(\boldsymbol{r},t) = -\frac{\omega^2}{4\pi\epsilon_0 c^2}\frac{e^{i(kr-\omega t)}}{r^3}(\boldsymbol{r}\times\boldsymbol{\mu})\times\boldsymbol{r} \quad (6)$$

in the far field ($|\boldsymbol{r}| \gg \lambda$), where $\boldsymbol{\mu} = \mu\boldsymbol{e}_\mu$ is the complex vector amplitude of the electrical dipole and $k = 2\pi/\lambda$ where λ is the wavelength of the emitted light. The optical momentum density in the field can be defined as the Poynting vector [29]

$$\boldsymbol{P} = \frac{1}{2}\mathrm{Re}(\boldsymbol{E}^*\times\boldsymbol{H}). \quad (7)$$

The momentum density can be divided into two components that arise from the orbital and and spin angular momentum of the field

$$\boldsymbol{p}_{\mathrm{orb}} = \frac{c^2\epsilon_0}{2\omega}\mathrm{Im}\left(\boldsymbol{E}^*\cdot\overrightarrow{\nabla}\boldsymbol{E}\right), \quad (8)$$

$$\boldsymbol{p}_{\text{spin}} = \frac{c^2\epsilon_0}{4\omega}\overrightarrow{\nabla} \times \text{Im}\left(\boldsymbol{E}^*\boldsymbol{E}\right). \quad (9)$$

From Eqs. (6) and (8), it is possible to derive an expression for the wavefronts, *i.e.* the surfaces normal to the $\boldsymbol{p}_{\text{orb}}$. In general, the wavefronts of elliptical dipoles in the x–y plane are kinky spirals given by

$$r(\phi) = \frac{1}{k}(\arctan[\epsilon \cdot \tan(\phi)] + \omega t) + \text{const}., \quad (10)$$

For a linearly polarized dipole ($\epsilon = 0$), *i.e.* a dipole with zero expectation value for its angular momentum, the wavefronts reduce to circles given by $r_{\text{wf}} = \frac{\omega t}{k} + \text{const}$, whereas for a $\sigma^{\pm}(\epsilon = \pm 1)$ polarized dipole that radiates waves with total angular momentum of $\pm\hbar$ per photon with respect to the z axis, the wavefronts in the x–y plane are given by

$$r_{\pm}(\phi) = \frac{\mp\phi + \omega t}{k} + \text{const}. \quad (11)$$

This corresponds to an Archimedean spiral rotating around the z axis, with the same rotation sense as the dipole. Supplementary Fig. 1 shows an example of the wavefronts of an elliptical dipole in comparison with the circular case.

Angular momentum and imaging

According to Eq. (8) the local orbital angular momentum can be calculated by applying the operator

$$\hat{\boldsymbol{L}} = \boldsymbol{r} \times \hat{\boldsymbol{p}}, \quad (12)$$

on the single-photon wavefunction, where $\hat{\boldsymbol{p}} = -i\hbar\overrightarrow{\nabla}$ is the orbital momentum density operator. The local orbital angular momentum per photon can be measured by sending the light through an aperture at position $\boldsymbol{r}_0$. We align the z-axis with the axis defined by the transverse angular momentum and define the optical axis as the x-axis. The expectation value of the transverse linear momentum component $\langle \hat{p}_y^w \rangle$ per photon at the position of the aperture is given by the displacement $\langle y \rangle$ of the centre of mass of the far-field image from the optical axis $\boldsymbol{e}_x$ at distance d from the aperture. The relation between angular momentum and displacement is given by

$$\langle y \rangle = \frac{d}{\hbar k}\langle \hat{p}_y^w \rangle = \frac{d}{\hbar k}\frac{1}{r_0}\langle \hat{L}_z^w \rangle. \quad (13)$$

This measurement can be interpreted in the framework of weak measurements, where the centre of mass in the image plane is proportional to the weak value of the photons' orbital angular momentum (or the transverse linear momentum) at the aperture, which are given at the position of the first lens by [29]

$$\left\langle \hat{L}_z^w \right\rangle = r_0 \cdot \left\langle \hat{p}_y^w \right\rangle = r_0 \cdot \frac{\left\langle \widetilde{\Psi}_{\text{post}} \left| \hat{p}_y \right| \Psi \right\rangle}{\left\langle \widetilde{\Psi}_{\text{post}} \mid \Psi \right\rangle}, \quad (14)$$

where $|\Psi\rangle$ and $|\widetilde{\Psi}_{\text{post}}\rangle$ are the initial wavefunction and the part of the wavefunction that passes the aperture (the post-selected state), respectively.

In other words, the orbital angular momentum components transverse to the optical axis result in a transverse linear momentum at the aperture that leads in turn to a displacement of the centre of mass of the diffracted beam in the far field. The local angular momentum per photon can exceed $\hbar$ where the field is weak (so-called 'supermomentum') [28].

Calculation of the image centroid

To obtain the displacement of the centroid of the image, we start with the above relation between angular momentum and transverse linear momentum. The considered imaging system consists of an objective with focal length f and aperture diameter D located at a distance f from the emitter. The electric fields of the three elementary dipoles π, σ^+ and σ^- at the objective are, for small aperture ($D \ll f$) and up to a common normalization constant, given by

$$\widetilde{\Psi}_{\pi}(\rho, \phi) = \frac{1}{f} \boldsymbol{e}_z e^{i\varphi}, \quad (15)$$

$$\widetilde{\Psi}_{\sigma^\pm}(\rho, \phi) = \frac{1}{\sqrt{2}} \left(\pm \frac{i}{f} \boldsymbol{e}_y + \frac{\rho}{f^2} \boldsymbol{e}_\rho \right) e^{i\varphi}, \quad (16)$$

where ρ and ϕ (y and z) are polar (Cartesian) coordinates in the aperture plane, $\boldsymbol{e}_x$, $\boldsymbol{e}_y$, $\boldsymbol{e}_z$ and $\boldsymbol{e}_\rho$ are the unit vectors in the respective direction, $\varphi = k\sqrt{\rho^2 + f^2}$. Since the emitter is in the focal plane of the objective, the latter applies the transformation $e^{-i\varphi}$ on the light and removes the phase factor in Eqs. (15) and (16) which we drop in the following. As a consequence, the phase fronts are transformed into plane waves while the average wavevector and the average transverse momentum are conserved. Measuring the displacement of the waveform's centre of mass from the optical axis $\langle q \rangle$ at distance d from the objective ($d \gg D$) then corresponds to a measurement of the expectation value of the transverse angular momentum component per photon $\langle \hat{L}_z^w \rangle$ or the linear transverse

momentum component $\langle \hat{p}_q^w \rangle$ of the photons at the position of the aperture where $q \in \{y, z\}$. The actions of the momentum operators on the wave are

$$\hat{p}_q \widetilde{\Psi}_{\sigma^\pm} = \pm \frac{i\hbar}{f^2\sqrt{2}} e_q, \quad (17)$$

as well as $\hat{p}_q \widetilde{\Psi}_\pi = 0$, Considering the general case of a photon that originates from a superposition of σ^+ and σ^- emission,we can calculate the weak value in Eq. (14) and obtain

$$\langle \hat{p}_y^w \rangle_r = \frac{\hbar}{f} \frac{\Re(\epsilon)}{1 + |\epsilon|^2 \mathrm{NA}^2/2}, \quad (18)$$

$$\langle \hat{p}_z^w \rangle_r = 0, \quad (19)$$

where we defined the numerical aperture as NA = $D/(2f)$. We note, that in general the expectation values $\langle \hat{p}_q^w \rangle$ are complex as ϵ can be a complex number. Since only the real part of the expectation values corresponds to a displacement of the image centroid, eqs. (18) and (19) only give the real part of the expectation $\langle \hat{p}_q^w \rangle$ which we denote by $\langle \cdot \rangle_r$.

In a microscopy set-up, the image is not formed at infinity, but a second lens with focal length f', which we assume to be at a distance f' from the aperture, is used to form an image at distance $2f'$ from the aperture. In this case, the expected displacement is obtained by replacing d by f'. This finally yields for the expected displacement on the screen

$$\langle \hat{y} \rangle = \frac{1}{\hbar k} \frac{f'}{f} \langle \hat{L}_y^w \rangle = \frac{\lambda}{2\pi} \frac{f'}{f} \frac{\Re(\epsilon)}{1 + |\epsilon|^2 \mathrm{NA}^2/2}. \quad (20)$$

For small numerical aperture (NA $\ll |\epsilon|$) and ϵ real, the displacement of the centroid increases linearly in ϵ. For circular polarization $\epsilon = \pm 1$, the centroid of the image is displaced from the expected position by $\langle \hat{y} \rangle \approx \pm\lambda/(2\pi)$ times the magnification of the optical system f'/f, *i.e.*, the particle appears to be displaced by $\mp\lambda/(2\pi)$, taking into account that the assumed imaging system produces a flipped image. The maximum displacement of the centroid for ϵ real is given by

$$\langle \hat{y} \rangle_{\max} = \pm \frac{\lambda}{2\pi} \frac{f'}{f} \frac{1}{\sqrt{2}\mathrm{NA}}, \quad (21)$$

i.e., for vanishing numerical aperture, the displacement of the apparent and real positions of the particle can be arbitrarily large.

Fourier-optic derivation of the centroid position

The position of the centroid can also be calculated in the framework of Fourier-optics. We calculate the electric fields of the three fundamental electrical dipoles oscillating in x, y and z directions in the image plane and obtain for the approximation of small NA

$$\boldsymbol{E}_x = -iE_0 \cdot \frac{\mathrm{NA}^2}{\rho} J_2(\tilde{\rho})(\cos\varphi \boldsymbol{e}_y + \sin\varphi \boldsymbol{e}_z), \quad (22)$$

$$\boldsymbol{E}_y = E_0 \cdot \frac{\mathrm{NA}}{\rho} J_1(\tilde{\rho}) \boldsymbol{e}_y, \quad (23)$$

$$\boldsymbol{E}_z = E_0 \cdot \frac{\mathrm{NA}}{\rho} J_1(\tilde{\rho}) \boldsymbol{e}_z, \quad (24)$$

where we have defined the amplitude

$$E_0 = \frac{\mu\omega^2}{4\pi\,\epsilon_0^2\,c^2}, \quad (25)$$

and $\tilde{\rho} = \rho \cdot k \cdot \mathrm{NA} \cdot f/f'$, with the opening angle of the objective NA $\approx D/(2f)$. The final image is then a superposition of the three dipole fields from which we obtain for the centroid again Eq. (20).

Immersion microscopy

In high-NA imaging, the so-called immersion method is used, where the first lens of the system is a solid immersion lens and the imaged particles are located on the planar side of the lens and embedded in immersion fluid that has the same refractive index as the lens. Consequently, wavefronts emitted by the particle are parallel to the surface of the lens. Thus, this method does not affect the wavefronts in the far field outside the lens and our discussion also applies for this case. It is only necessary to replace the numerical aperture NA with the geometrical numerical aperture NA_g ($\mathrm{NA}_g = \mathrm{NA}/n$) and to replace λ with the wavelength in the immersion fluid λ/n.

Atomic transition selective detection of photons

In the atom experiment, the photons are emitted with angular momentum $\Delta m\hbar$ from a dipole transition of a single $^{138}Ba^+$ atomic ion in a Paul trap, where Δm is given by the difference in the magnetic quantum number of the electronic level before and after the photon

emission. $\Delta m = 0$ corresponds to emission from a linear π dipole and $\Delta m = \pm 1$ to emission from a circular $\sigma^{\mp}$ dipole. Photons are emitted from the cooling transition, with $\lambda = 493.41$ nm (Supplementary Fig. 5a). A magnetic field $B = 0.45$ mT parallel to the axis of the trap (z axis) defines the quantization axis perpendicular to the optical axis (x axis). The ion is Doppler-cooled, reducing the extension of the motional atomic wavepacket down to ~ 36 nm, then optically pumped into one of the Zeeman levels of the $6S_{1/2}$ ground state. For example, when preparing a photon emission $\Delta m = +1$, we pump to the $6S_{1/2}$, $m_j = -1/2$ with a σ^--polarized 493 nm laser and a repumper beam. Subsequently, we apply a short σ^+-polarized 493 nm laser pulse which excites the atom to the state $6P_{1/2}$, $m_j = +1/2$ (Supplementary Fig. 5b, d). From that excited state, the atom can spontaneously decay back to $6S_{1/2}$, $m_j = -1/2$ through a $\Delta m = +1$ transition, to $6S_{1/2}$, $m_j = +1/2$ through a $\Delta m = 0$ transition, or to the $6D_{3/2}$ manifold. During this transition the atom emits a photon that can be collected by the objective (NA = 0.40) and directed to the camera through the imaging system. To detect photons from the opposite transition ($\Delta m = -1$), the polarization of the optical pumping and excitation beams are exchanged (Supplementary Fig. 5c).

In this configuration, photons from $\Delta m = 0$ ($\Delta m = \pm 1$) transition are horizontally (vertically) polarized along the optical axis. This allows us to select only photons from the σ ($\Delta m = \pm 1$) transitions by introducing a polarization beam splitter (PBS) after the objective. An ideal PBS removes 99.998% of photons from the π transitions and 2.7% of photons from the σ transitions. Therefore we expect that the $\sigma^{\pm}$ dipole image is not significantly changed by the polarization filtering, and indeed this is borne out by complete numerical simulations (Supplementary Fig. 6).

The results shown in the main text were obtained using an intensified CCD camera (ICCD, Andor iStar A-DH334T-18H-63). Supplementary Fig. 5d shows the sequence and timing used in the experiment.

Atom image characteristics, stability and drifts correction

The image of the atomic ion corresponds to the PSF of the imaging system which is well approximated in our case by a 2D Gaussian. The detected images are fitted to a Gaussian profile with seven free parameters (z_0, y_0, σ_z, σ_y, A, O, θ), being (z_0, y_0) the coordinates of the centroids, σ_z and σ_y the standard deviation in the major and minor axis, A the amplitude, O an offset and θ rotation angle with respect to the CCD sensor axis. The magnification of the imaging system is measured by imaging a string of two ions separated by well-known distance [42], and is given by $M = 5.40(7)$.

The long accumulation time introduces a new source of error in the position estimation from mechanical drifts in the imaging system. The stability of the imaging system is characterized by the Allan variance of the fitted centroids of the detected images [7], which gives us a measure of the position uncertainty depending on the accumulation time τ. This is done by taking N pictures with exposure time t, adding them in bins of duration $\tau = nt$, where n is a integer number smaller than $N/2$. Each binned image is fitted to the seven parameter Gaussian function, from where the centroids are extracted. For comparison we also use, besides the ICCD camera, an EMCCD camera (Andor iXon DU-897) with bigger pixel size ($16 \times 16\ \mu m^2$). In the case of the EMCCD camera we take 2000 images of 2 s exposure time

with the atom emitting resonance florescence at maximum rate. In the case of the ICCD camera, we take 3000 images of 0.5 s exposure. In both cases, the time between two consecutive images is negligible. Supplementary Fig. 7a, b shows the vertical position uncertainty extracted with this method. The minimum uncertainty in the vertical position obtained using the EMCCD camera is 2.13(41) nm for 148 s accumulation time, while for the ICCD set-up the minimum is 3.29(71) nm for 74 s accumulation time. In both cases the decreasing part of the curve is dominated by shot noise. The drift of the centre of the fitted reference images used in the experiment is shown in Supplementary Fig. 7c where we observe that in a period of 3 h the image drifts a maximum of ~ 200 nm in both vertical and horizontal directions. To compensate for these drifts, we use the acquisition of long-exposure images during the cooling stage (Supplementary Fig. 5e) to obtain a real-time 'reference' of the particle position. Supplementary Figs. 5d, e show the full experimental sequence. This sequence is repeated for 3 h, and the analysed pictures correspond to accumulation of photons in a 11 × 11 pixel sub-area of the CCD sensor.

After the data collection is finished, each reference image is fitted, and the mean centroid position of two consecutive reference images is used to correct for the drifts in the signal image acquired between them. Then, we add up all the corrected signal images and fit these data. Finally, we compare the centroid positions of the added-up reference and signal images to determine their relative displacement. The uncertainty of the displacement is extracted from the 1σ confidence intervals using χ^2 analysis, given its relation with the real noise sources [43].

Nanoparticle sample preparation and set-up

We deposit a single gold nanoparticle (BBI solutions, diameter 100 nm) on a silica nanofibre (diameter 410 nm) by touching the nanofibre with a droplet, that contains a diluted suspension of nanoparticles. The presence of a single nanoparticle on the nanofibre can be detected via absorption spectroscopy [34]. The solid immersion lenses are positioned around the nanoparticle, such that the nanoparticle lies in the centre of the two lenses. The gap between the lenses of about 200 μm is filled up with immersion oil.

The imaging system is a combination of a long working distance microscope and the solid immersion lenses (half ball lenses with a radius of 2.5 mm). The microscope consists of an infinity corrected objective by Mitutoyo, with a magnification of 20 and an infinity tube lens to image onto a CCD camera (Matrix Vision mvBlueFOX3-1013G-2212). In two different measurements we used two different objectives with the numerical apertures of NA = 0.28 and NA = 0.42. Via a surface topography standard, we measure the magnification of the long working distance microscope. This combination results in an overall imaging system with numerical apertures NA = 0.41 and NA = 0.61 and the magnifications $M_{0.41}$ = 21.9(2) and $M_{0.61}$ = 20.1(1).

In the experiment we use two laser beams: a reference and a measurement beam, with fixed and adjustable polarization respectively, see Fig. 2b. The polarization of the reference beam is aligned along the z axis. The measurement beam is set to be linear polarized along the y axis before passing through a half- and then a quarter-wave plate. By rotating the half-wave plate we can adjust the beam's polarization to every elliptical polarization with the major

axes along x or y. In order to avoid aberration caused by light propagating along the ridge of the two immersion lenses, the measurement beam is tilted by 7° degrees from the z axis, see Fig. 2b. This tilt is included in the theory plots shown in Fig. 3f.

Data acquisition and analysis

The illumination times of the images are 2 ms (NA = 0.41 objective) and 6.5 ms (NA = 0.61 objective). The pictures are taken alternately using the reference and measurement beams (Fig. 2b). In the experimental sequence, the particle displacements are measured as a function of polarization and the focal position of the imaging optics. For every polarization ratio ϵ, the relative focus position is scanned by moving the long working distance microscope with a step size of 1.25 μm and a total range ~ 20 μm. Then, the polarization ratio is changed by rotating the half-wave plate by 2.5°. 25 tuples of data are acquired for every ϵ and focus position. Fig. 3f shows the mean displacements obtained from averaging over all displacements for the five focal positions closest to the focus of the imaging system. The statistical error of each data point displayed in Fig. 3f is estimated as $\sigma_{\Delta y}/\sqrt{125}$, where $\sigma_{\Delta y}$ is the standard deviation of the measured displacements.

To correct for inhomogeneous pixel efficiencies of the CCD camera, we apply standard flat-field correction on the measured image data. Then, in order to determine the (apparent) position of the nanoparticle, we fit a 2D Gaussian with six free fit parameters to the particle images. The free parameters are the centroid position (z_0, y_0), the amplitude A, the waists σ_z and σ_y of the elliptical Gaussian and an intensity offset O.

Supplementary Material

Refer to Web version on PubMed Central for supplementary material.

Acknowledgements

We thank P. Obšil for his experimental support, and J. Enderlein, M. Hush and A. Jesacher for helpful discussions. This work has been supported by the Austrian Science Fund (FWF, SINPHONIA project P23022, SFB FoQuS F4001, SFB NextLite F4908), by the European Research Council through project CRYTERION #227959, by the Institut für Quanteninformation GmbH, and by the Australian Research Council through project CE170100012.

References

[1]. Boas, DA, Pitris, C, Ramanujam, N. Handbook of biomedical optics. CRC press; 2011.

[2]. Kovalevsky, J, Seidelmann, PK. Fundamentals of astrometry. Cambridge University Press; 2004.

[3]. Novotny, L, Hecht, B. Principles of Nano-Optics. Cambridge University Press; 2006.

[4]. Anderson J, King IR. Toward high-precision astrometry with WFPC2. I. deriving an accurate point-spread function. Publ Astron Soc Pac. 2000; 112:1360–1382.

[5]. Hell SW. Far-field optical nanoscopy. Science. 2007; 316:1153–1158. [PubMed: 17525330]

[6]. Alberti A, et al. Super-resolution microscopy of single atoms in optical lattices. New J Phys. 2016; 18

[7]. Wong-Campos JD, Johnson KG, Neyenhuis B, Mizrahi J, Monroe C. High-resolution adaptive imaging of a single atom. Nature Photon. 2016; 10:606–610.

[8]. Sapienza L, Davanço M, Badolato A, Srinivasan K. Nanoscale optical positioning of single quantum dots for bright and pure single-photon emission. Nat Commun. 2015; 6

[9]. Thompson RE, Larson DR, Webb WW. Precise nanometer localization analysis for individual fluorescent probes. Biophys J. 2002; 82:2775. [PubMed: 11964263]

[10]. Enderlein J, Toprak E, Selvin PR. Polarization effect on position accuracy of fluorophore localization. Opt Express. 2006; 14:8111–8120. [PubMed: 19529183]

[11]. Engelhardt J, et al. Molecular orientation affects localization accuracy in superresolution far-field fluorescence microscopy. Nano Lett. 2011; 11:209–213. [PubMed: 21133355]

[12]. Backlund MP, et al. Simultaneous, accurate measurement of the 3D position and orientation of single molecules. Proc Natl Acad Sci U S A. 2012; 109:19087–19092. [PubMed: 23129640]

[13]. Lew MD, Moerner WE. Azimuthal polarization filtering for accurate, precise, and robust single-molecule localization microscopy. Nano Lett. 2014; 14:6407–6413. [PubMed: 25272093]

[14]. Backlund MP, et al. Removing orientation-induced localization biases in single-molecule microscopy using a broadband metasurface mask. Nature Photon. 2016; 10:459–464.

[15]. Mortensen KI, Churchman LS, Spudich JA, Flyvbjerg H. Optimized localization analysis for single-molecule tracking and super-resolution microscopy. Nat Methods. 2010; 7:377–381. [PubMed: 20364147]

[16]. Quirin S, Pavani SRP, Piestun R. Optimal 3D single-molecule localization for superresolution microscopy with aberrations and engineered point spread functions. Proc Natl Acad Sci U S A. 2012; 109:675–679. [PubMed: 22210112]

[17]. Stallinga S, Rieger B. Position and orientation estimation of fixed dipole emitters using an effective Hermite point spread function model. Opt Express. 2012; 20:5896–5921. [PubMed: 22418467]

[18]. Wertz E, Isaacoff BP, Flynn JD, Biteen JS. Single-molecule super-resolution microscopy reveals how light couples to a plasmonic nanoantenna on the nanometer scale. Nano Lett. 2015; 15:2662–2670. [PubMed: 25799002]

[19]. Raab M, Vietz C, Stefani FD, Acuna GP, Tinnefeld P. Shifting molecular localization by plasmonic coupling in a single-molecule mirage. Nat Commun. 2017; 8

[20]. Moe G, Happer G. Conservation of angular momentum for light propagating in a transparent anisotropic medium. J Phys B At Mol Phys. 1977; 10:1191–1208.

[21]. Schwartz C, Dogariu A. Conservation of angular momentum of light in single scattering. Opt Express. 2006; 14:8425–8433. [PubMed: 19529220]

[22]. Bliokh KY, Rodríguez-Fortuno FJ, Nori F, Zayats AV. Spin-orbit interactions of light. Nature Photon. 2016; 9:796–808.

[23]. Bliokh KY, Gorodetski Y, Kleiner V, Hasman E. Coriolis effect in optics: Unified geometric phase and spin-Hall effect. Phys Rev Lett. 2008; 101

[24]. Rodríguez-Herrera OG, Lara D, Bliokh KY, Ostrovskaya EA, Dainty C. Optical nanoprobing via spin-orbit interaction of light. Phys Rev Lett. 2010; 104

[25]. Lodahl P, et al. Chiral quantum optics. Nature. 2017; 541:473–480. [PubMed: 28128249]

[26]. Li X, Arnoldus HF. Macroscopic far-field observation of the sub-wavelength near-field dipole vortex. Phys Lett A. 2010; 374:1063–1067.

[27]. Darwin CG. Notes on the theory of radiation. Proc Royal Soc A. 1932; 136:36–52.

[28]. Bekshaev AY, Bliokh KY, Nori F. Transverse spin and momentum in two-wave interference. Phys Rev X. 2015; 5

[29]. Berry MV. Optical currents. J Opt A: Pure Appl Opt. 2009; 11

[30]. Knee GC, Combes J, Ferrie C, Gauger EM. Weak-value amplification: state of play. Quantum Meas and Quantum Metrol. 2016; 3:32–37.

[31]. Stallinga S, Rieger B. Accuracy of the Gaussian point spread function model in 2D localization microscopy. Opt Express. 2010; 18:24461–24476. [PubMed: 21164793]

[32]. Howes PD, Chandrawati R, Stevens MM. Colloidal nanoparticles as advanced biological sensors. Science. 2014; 346

[33]. Zhang P, Lee S, Yu H, Fang N, Kang SH. Super-resolution of fluorescence-free plasmonic nanoparticles using enhanced dark-field illumination based on wavelength-modulation. Sci Rep. 2015; 5

[34]. Petersen J, Volz J, Rauschenbeutel A. Chiral nanophotonic waveguide interface based on spin-orbit interaction of light. Science. 2014; 346:67–71. [PubMed: 25190718]

[35]. Yildiz A, et al. Myosin V walks hand-over-hand: single fluorophore imaging with 1.5-nm localization. Science. 2003; 300:2061–2065. [PubMed: 12791999]

[36]. Small AR, Parthasarathy R. Superresolution localization methods. Annu Rev Phys Chem. 2014; 65:107–125. [PubMed: 24274701]

[37]. Bakr WS, Gillen JI, Peng A, Folling S, Greiner M. A quantum gas microscope for detecting single atoms in a Hubbard-regime optical lattice. Nature. 2009; 462:74–77. [PubMed: 19890326]

[38]. Lee, J-S, Pottier, E. Polarimetric radar imaging: from basics to applications. CRC press; 2009.

[39]. Hayes MP, Gough PT. Synthetic aperture sonar: A review of current status. IEEE J Ocean Eng. 2009; 34:207–224.

[40]. Abbott BP, et al. Search for post-merger gravitational waves from the remnant of the binary neutron star merger GW170817. Astrophys J Lett. 2017; 851:L16.

[41]. Bialynicki-Birula I, Bialynicka-Birula Z. Gravitational waves carrying orbital angular momentum. New J Phys. 2016; 18

[42]. James D. Quantum dynamics of cold trapped ions with application to quantum computation. Appl Phys B. 1998; 66:181–190.

[43]. Bobroff N. Position measurement with a resolution and noise-limited instrument. Rev Sci Instrum. 1986; 57:1152–1157.

Europe PMC Funders Author Manuscripts

Europe PMC Funders Author Manuscripts

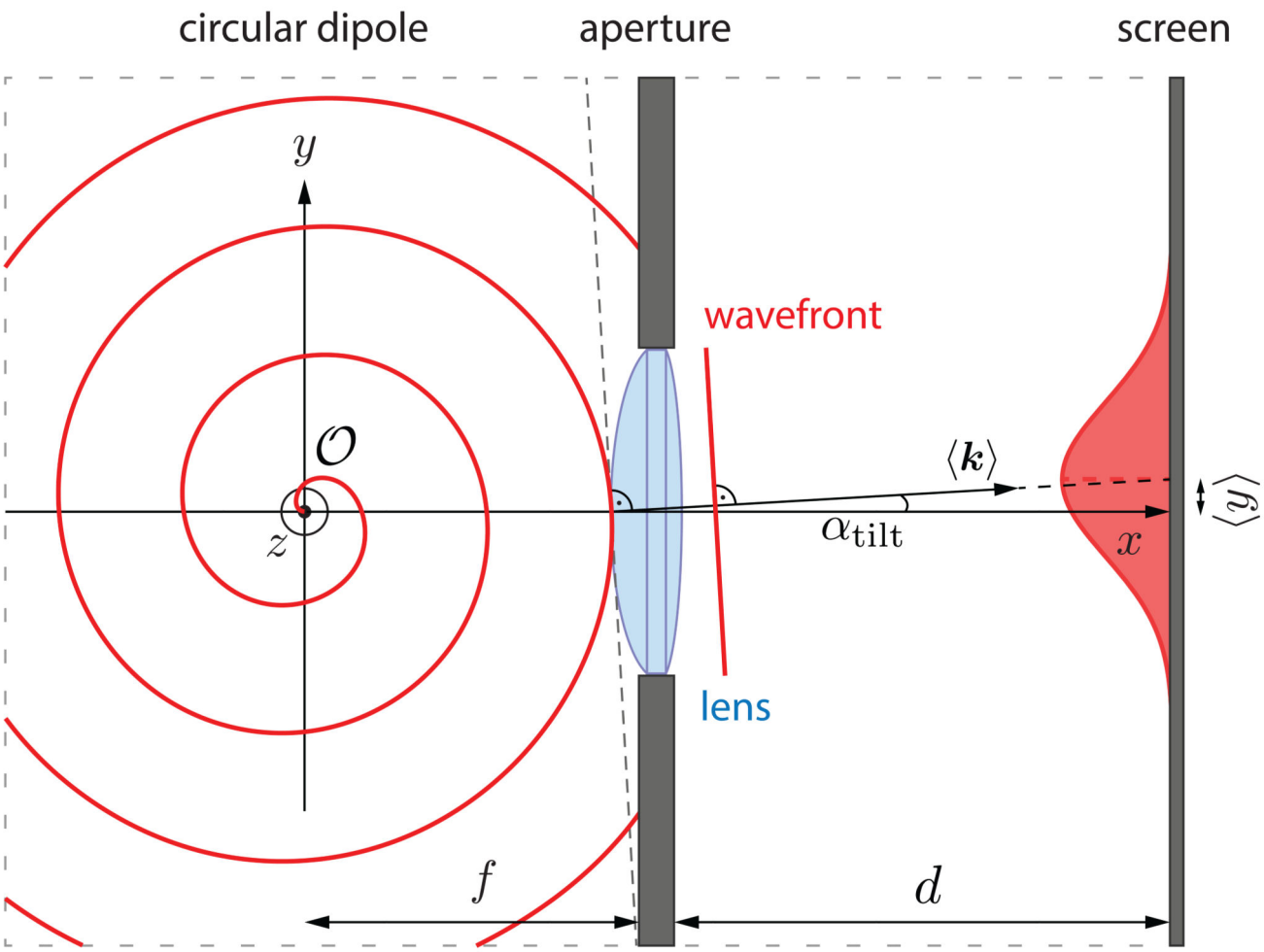

Figure 1. Polarization-dependent displacement.

A σ^+ rotating dipole located at $\mathcal{O}$ emits spiral wavefronts in the equatorial x–y plane, which are collimated by a lens with focal length f centred on the x axis and focused on the dipole. The wavefronts passing through the aperture of the lens have a mean wavevector $\langle \boldsymbol{k} \rangle$ tilted by an angle α_{tilt} with respect to the x axis, which shifts the intensity distribution by $\langle y \rangle$ after a propagation length d. This shift originates from an orbital angular momentum of $\hbar$ per photon and results in an apparent displacement $\Delta y = -\lambda/2\pi$ of the emitter (see text). For a σ^- emission the shift occurs in the opposite direction, since the wavefronts spiral in the opposite way. For elliptically polarized dipoles, even lager shifts and larger tilts of the wavefronts can arise, see Supplementary Fig. 1.

Europe PMC Funders Author Manuscripts

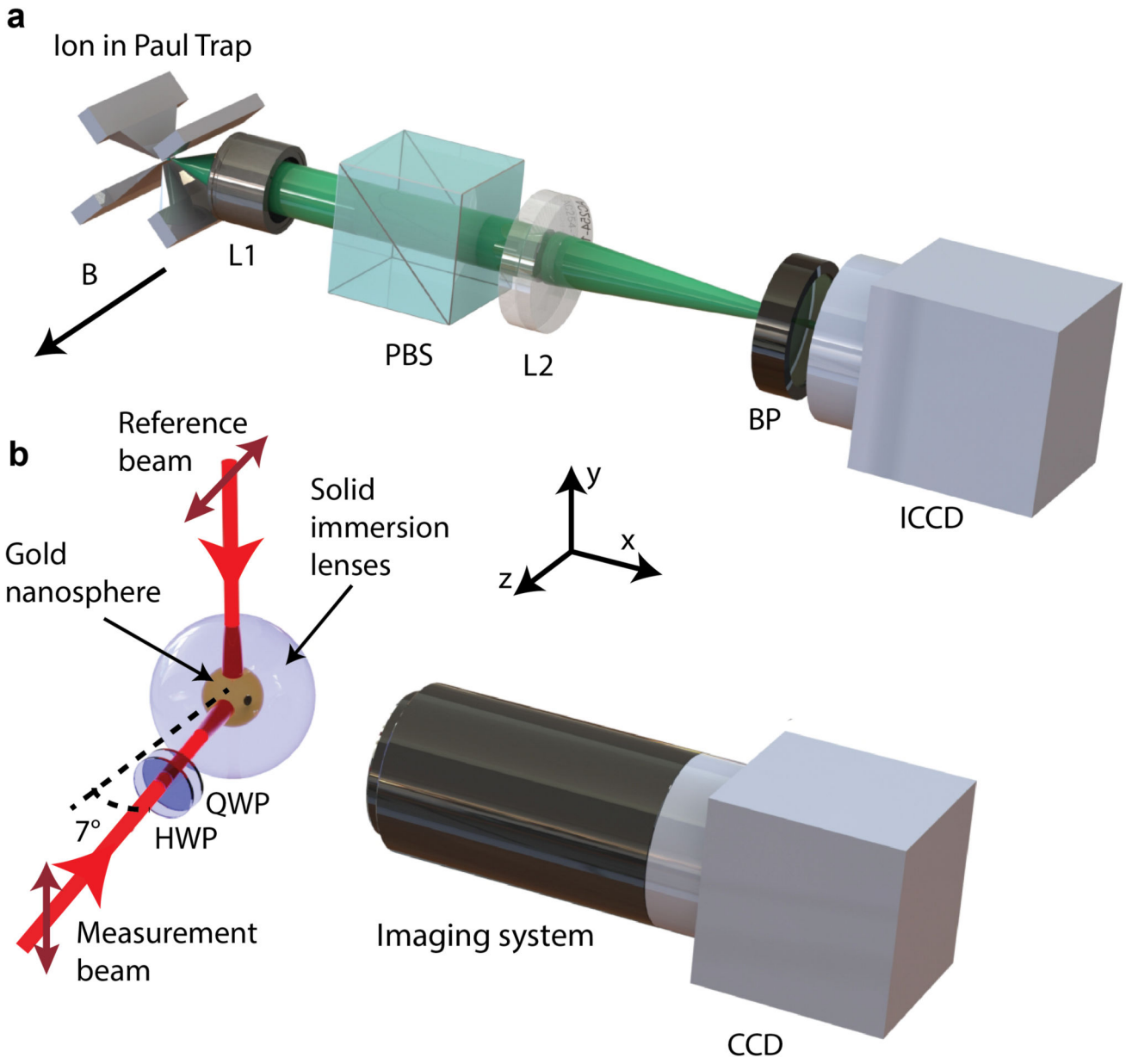

Figure 2. Experimental set-ups.

a, A $^{138}Ba^{+}$ ion is confined in a linear Paul trap. A magnetic field **B** along $\hat{z}$ defines the quantization axis and the rotation axis of the dipoles. Fluorescence light is collected in the $\hat{x}$ direction by an in-vacuum objective (L1, focal length: 25 mm, NA=0.40), and a lens (L2, focal length 150 mm) forms a focus on an intensified CCD camera (ICCD). A polarization beam splitter (PBS) filters out photons with polarization parallel to the quantization axis (π-polarized photons), while a bandpass filter (BP) selects photons with wavelength 493 $\pm$ 1 nm. **b,** A gold nanosphere is located in the gap between two solid immersion lenses, filled with index matching oil to prevent reflections. The particle scatters light alternatively from a reference beam with fixed linear polarization and a measurement beam whose polarization is

adjusted using half- (HWP) and quarter-wave (QWP) plates. The scattered light is collected by a microscope objective and imaged onto a CCD camera.

Europe PMC Funders Author Manuscripts

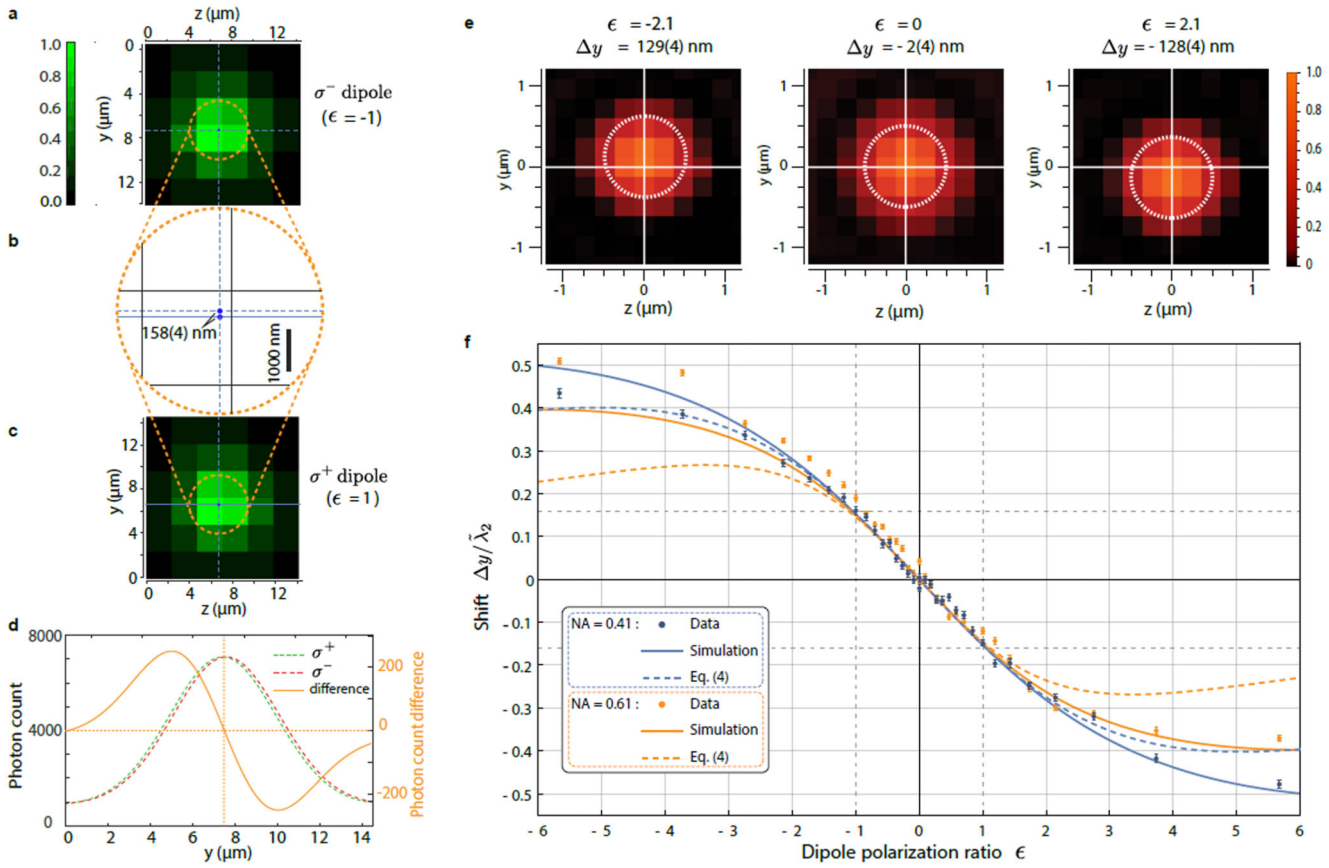

Figure 3. Apparent displacement of the emitters.

a, c, Measured images (normalized to maximum pixel count rate) of a single atom for the σ^- and σ^+ transitions. The blue lines and blue points indicate the centroid of the image obtained by a 2D Gaussian fit to the data. The orange circle represents the 1σ-width. **b,** Zoom of the centre of images **a** and **c**. The two blue points show the centroid position of the fitted σ^- (upper point) and σ^+ (lower point) images. **d,** Vertical cross section of the Gaussian fits for σ^+ (green dashed curve, left scale) and σ^- (red dashed curve, left scale) polarizations. The orange curve shows the difference of both fits (right scale). **e,** Measured images of the nanoparticle for $\epsilon = \pm 2.1$ and $\epsilon = 0$ for NA = 0.41. The white cross indicates the position of the nanoparticle obtained from the reference image. The dashed circle with a diameter of 500 nm indicates the 1σ width of the image obtained from a Gaussian fit and is centred around the apparent position of the nanoparticle. **f,** Relative displacement of the image of the particle as a function of ϵ, measured for two different NAs. The error bars indicate the standard deviation of the 125 individual position measurements for each data point. The dashed curves are the theoretical predictions of Eq. (4) and the solid curves are the displacements obtained by simulations of the image process taking into account that the centroid of the images are obtained from a Gaussian fit (see Methods). The dashed grey lines show the case of circularly polarized emitters.

Europe PMC Funders Author Manuscripts